

# Signatures of Kondo-Majorana interplay in $ac$ response

Krzysztof P. Wójcik,<sup>1,2,\*</sup> Tadeusz Domański,<sup>2,†</sup> and Ireneusz Weymann<sup>3,‡</sup>

<sup>1</sup>*Institute of Molecular Physics, Polish Academy of Sciences, Smoluchowskiego 17, 60-179 Poznań, Poland*

<sup>2</sup>*Institute of Physics, Maria Curie-Skłodowska University, 20-031 Lublin, Poland*

<sup>3</sup>*Institute of Spintronics and Quantum Information, Faculty of Physics, Adam Mickiewicz University, 61-614 Poznań, Poland*

(Dated: October 2, 2024)

We analyze dynamical transport properties of a hybrid nanostructure, comprising a correlated quantum dot embedded between the source and drain electrodes, which are subject to an  $ac$  voltage, focusing on signatures imprinted on the charge transport by the side-attached Majorana zero-energy mode. The considerations are based on the Kubo formula, for which the relevant correlation functions are determined by using the numerical renormalization group approach, which allows us to consider the correlation effects due to the Coulomb repulsion and their interplay with the Majorana mode in a non-perturbative manner. We point out universal features of the dynamical conductance, showing up in the Kondo-Majorana regime, and differentiate them against the conventional Kondo and Majorana systems. In particular, we predict that the Majorana quasiparticles give rise to universal fractional values of the  $ac$  conductance in the well-defined frequency range below the peak at the Kondo scale. We also show this Kondo scale to actually increase with strengthening the coupling to the topological superconducting wire.

## I. INTRODUCTION

Dynamical transport properties, such as shot noise or  $ac$  response, give valuable information about the charge carriers and can provide evidence for their unique character [1]. They are hence useful for exploring the exotic phases of matter [2–5] and for uncovering the subtle fingerprints of interactions [6–12]. The dynamical properties can be also studied with optical means [13, 14], including the quantum dots (QDs) coupled to microwave cavities [15–18], where they provide insight into photon-assisted transport [19] or inelastic scattering processes [20, 21]. Measurements of dynamical transport properties have been so far reported, both for the normal [22, 23] and superconducting nanostructures [24, 25] and they are nowadays attainable with unprecedented precision [26], opening up the field for new exciting experiments.

In particular, the dynamical response studies could be adopted to identify unique signatures of hybrid nanostructures with topological superconductors (TSSs), harboring the Majorana quasiparticles. Fluctuations of the charge currents through various arrangements of TSSs and QDs attached to them have been recently studied, focusing on the shot noise [27–31] and coupling to a microwave cavity [32–37]. Moreover, dynamical properties of the Majorana bound states have been analyzed by the nonequilibrium Keldysh formalism, determining the finite frequency emission and absorption noise to all orders in the tunneling amplitude through a biased junction between a normal metal and topological superconductor [38]. Peculiarities of the Majorana noise have been also inspected for the spinless (Kitaev) counterpart of the

setup studied here, demonstrating its universal features manifested by resonances and antiresonances appearing at characteristic frequencies [39]. Such studies provided information about less conventional signatures of Majorana quasiparticles, which are complementary to their zero-energy static features reported in the tunneling measurements [40–42] and quench dynamics [43–45]. Vast majority of these studies, however, focused on spinless theories, neglecting the Coulomb repulsion responsible for the correlation phenomena.

In this paper we investigate dynamical hallmarks of the Majorana mode coupled to the strongly correlated quantum dot that would be observable in charging-discharging processes driven by the external  $ac$  field. For microscopic considerations we choose the single dot hybrid structure, displayed in Fig. 1. Here proposed methodology can be naturally extended to other, more complex structures. As an example, we point out some alternative realization of our model (see Appendix A), where specific contribu-

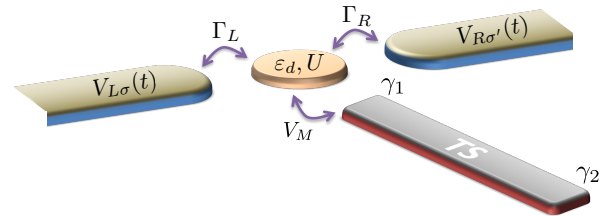


Figure 1. Schematic of the hybrid setup with a correlated quantum dot placed between the external (left and right) electrodes and side-coupled to the topological superconducting (TS) nanowire, hosting the Majorana end-modes (described by  $\hat{\gamma}_1$  and  $\hat{\gamma}_2$ ). The quantum dot is characterized by the energy level  $\varepsilon_d$  and the Coulomb potential  $U$ . The dynamical charge transport is driven by time-dependent voltage  $V_{j\sigma}(t)$  applied between the contacts.

\* kpowojcik@ifmpan.poznan.pl

† doman@kft.umcs.lublin.pl

‡ weymann@amu.edu.pl

tions of the dynamical conductance could be examined without spin-resolved measurements.

Hybridization of the quantum dot with a topological superconducting wire gives rise to a leakage of the Majorana boundary mode onto the side-attached QD [46]. When confronted with the Coulomb interactions it develops the unique *Kondo-Majorana* (KM) strong coupling low-energy fixed point [47–49] characterized by universal spin-asymmetric spectral density [50], resembling the one in non-interacting systems, yet revealing a fully-screened impurity magnetic moment [51]. The latter seems difficult to be measured directly, whereas the static *dc*-transport features of such KM fixed point are hardly distinguishable from those of noninteracting Majorana-quantum dot hybrid systems [52–55]. Here we show that *ac* transport properties would be a suitable tool to discriminate them.

In what follows, we analyze the universal *ac* conductance over extended range of frequencies, bounded from above by the energy scale corresponding to the Majorana coupling,  $\omega_{\max} \sim 2\Gamma_M$ , and from below by the scale related to the overlap of Majorana modes,  $\varepsilon_M$ , encountered in short-length topological superconducting systems,  $\omega_{\min} \sim \varepsilon_M(1 + \Gamma_M/\varepsilon_M)^{-1}$ . Here,  $\Gamma_M \approx 2V_M^2/\Gamma$ , where  $V_M$  is the matrix element between the QD and TS, while  $\Gamma$  denotes the coupling strength to the left and right leads. In the case of long topological superconducting nanowire,  $\varepsilon_M \rightarrow 0$ , the universal feature corresponds to the zero-bias peak, and  $\omega_{\max}$  is the maximal *ac* frequency allowing for its observation. Taking the Coulomb interaction effects into account, we carefully investigate what dynamical response characterizes the Kondo-Majorana fixed point, which (to the best of our knowledge) is still awaiting its experimental observation. With the present paper we aim to provide means of such detection.

The paper is organized as follows. In Sec. II we introduce the model and describe the numerical methods, based on numerical renormalization group (NRG) technique [56] and Kubo formalism [57]. Section III discusses the relevant energy scales, inferred from analysis of all contributions to the response functions. Then, Sec. IV combines these contributions into differential conductance of the device for various biasing scenarios. In Sec. V we briefly discuss alternative methods capable to deal with correlation phenomena under *ac* nonequilibrium conditions. Finally, Sec. VI concludes our study. Additionally, Appendix A presents an alternative experimental setup for verification of our findings and Appendix B shows the results obtained when the topological superconductor is replaced by a conventional one.

## II. THEORETICAL DESCRIPTION

The considered nanostructure (Fig. 1) consists of a correlated quantum dot placed between two external leads and additionally coupled to a topological superconducting nanowire, hosting the Majorana boundary modes de-

scribed by the operators  $\hat{\gamma}_1$  and  $\hat{\gamma}_2$ , respectively. External leads are subject to a time-dependent bias voltage, inducing *ac* charge transport via the quantum dot. In what follows, we briefly specify the low-energy microscopic model of this system and present the theoretical framework for treating the dynamical phenomena within the linear-response theory.

### A. Hamiltonian

The system's Hamiltonian consists of the following terms

$$\hat{H} = \sum_{j=L,R} \left( \hat{H}_j + \hat{H}_{j\text{-QD}} \right) + \hat{H}_{\text{QDM}}. \quad (1)$$

The external electrodes are assumed to be reservoirs of the itinerant electrons

$$\hat{H}_j = \sum_{\sigma} \int [\varepsilon - \mu_{j\sigma}(t)] \hat{c}_{j\varepsilon\sigma}^{\dagger} \hat{c}_{j\varepsilon\sigma} d\varepsilon, \quad (2)$$

where  $\hat{c}_{j\varepsilon\sigma}^{\dagger}$  ( $\hat{c}_{j\varepsilon\sigma}$ ) denote the creation (annihilation) operators of spin- $\sigma$  electrons in  $j$ -th lead, which satisfy anticommutation relation  $\{\hat{c}_{j\varepsilon\sigma}^{\dagger}, \hat{c}_{j'\varepsilon'\sigma'}\} = \delta_{jj'}\delta_{\sigma\sigma'}\delta(\varepsilon - \varepsilon')$ , and  $\mu_{j\sigma}(t)$  is the corresponding time-dependent chemical potential. Electron tunneling between the  $j$ -th lead and the quantum dot is described by

$$\hat{H}_{j\text{-QD}} = \sum_{\sigma} \int \sqrt{\rho_j(\varepsilon)} \left( v_j \hat{d}_{\sigma}^{\dagger} \hat{c}_{j\varepsilon\sigma} + \text{H.c.} \right) d\varepsilon, \quad (3)$$

where  $v_j$  is the hopping matrix element and  $\rho_j(\varepsilon)$  is the density of states of  $j$ -th lead. Since our considerations refer to a narrow energy region (of a width  $\sim$  meV) inside the topological gap of superconducting nanowire, we assume the density of states to be flat,  $\rho_j(\varepsilon) = \rho \equiv 1/2D$ , where  $D$  is the band energy cut-off, used as a convenient energy unit throughout,  $D \equiv 1$ . The hybridization effects (3) can be taken into account by introducing the couplings  $\Gamma_j = \pi|v_j|^2\rho_j$ .

The last term of the Hamiltonian (1) describes the quantum dot combined with the Majorana modes of the TS [58, 59]

$$\begin{aligned} \hat{H}_{\text{QDM}} = & \varepsilon_d \sum_{\sigma} \hat{n}_{\sigma} + U \hat{n}_{\uparrow} \hat{n}_{\downarrow} \\ & + V_M (\hat{d}_{\downarrow}^{\dagger} - \hat{d}_{\downarrow}) \hat{\gamma}_1 + i\varepsilon_M \hat{\gamma}_1 \hat{\gamma}_2, \end{aligned} \quad (4)$$

where  $\hat{d}_{\sigma}^{\dagger}$  ( $\hat{d}_{\sigma}$ ) is the creation (annihilation) operator for spin- $\sigma$  electrons on the QD of energy  $\varepsilon_d$  and Coulomb correlations  $U$ ,  $\hat{n}_{\sigma} = \hat{d}_{\sigma}^{\dagger} \hat{d}_{\sigma}$  is the corresponding electron number operator, and  $\hat{\gamma}_{1,2}$  are the operators of the boundary zero-energy modes. Hybridization of the quantum dot spin- $\downarrow$  electrons with the left hand-side Majorana quasiparticle is denoted by  $V_M$ , while  $\varepsilon_M$  stands for an overlap between the Majorana modes. It is useful

to represent the Majorana operators  $\hat{\gamma}_i$  in terms of the conventional fermion operators  $\hat{f}_M^{(\dagger)}$ ,

$$\hat{\gamma}_1 = (\hat{f}_M + \hat{f}_M^\dagger)/\sqrt{2}, \quad (5a)$$

$$\hat{\gamma}_2 = -i(\hat{f}_M - \hat{f}_M^\dagger)/\sqrt{2}, \quad (5b)$$

which obey the standard anti-commutation relations.

## B. AC conductance

The charge current flowing from the  $j$ -th lead to the quantum dot in spin channel  $\sigma$  can be expressed by the operator  $\hat{I}_{j\sigma}(t) = e \partial_t \hat{N}_{j\sigma}(t)$ , where  $\hat{N}_{j\sigma} = \int \hat{c}_{j\epsilon\sigma}^\dagger \hat{c}_{j\epsilon\sigma} d\epsilon$  counts total number of spin- $\sigma$  electrons in the aforementioned lead, time argument indicates the Heisenberg picture, and  $e = |e|$  stands for the elementary charge. Assuming the topological superconductor to be grounded, the applied time-dependent voltage affects the chemical potentials of external leads as  $V_{j\sigma}(t) \equiv -\mu_{j\sigma}(t)/e$ . Within the linear-response Kubo formalism [57], it is useful to define the Fourier transform  $V_{j\sigma}(t) = (2\pi)^{-1} \int e^{-i\omega t} V_{j\sigma}(\omega) d\omega$ . The expectation value of the charge current,  $I_{j\sigma}(t) \equiv \langle \hat{I}_{j\sigma}(t) \rangle$ , can be then expressed in terms of the Fourier transforms by [8, 60]

$$I_{j\sigma}(\omega) = \sum_{j'\sigma'} \mathcal{G}_{jj'}^{\sigma\sigma'}(\omega) V_{j'\sigma'}(\omega), \quad (6)$$

with the system's admittance

$$\mathcal{G}_{jj'}^{\sigma\sigma'}(\omega) = \frac{i}{\omega} \left( \langle \langle \hat{I}_{j\sigma} | \hat{I}_{j'\sigma'} \rangle \rangle_\omega^{\text{ret}} - \langle \langle \hat{I}_{j\sigma} | \hat{I}_{j'\sigma'} \rangle \rangle_{\omega=0}^{\text{ret}} \right), \quad (7)$$

where  $\langle \langle \hat{I}_{j\sigma} | \hat{I}_{j'\sigma'} \rangle \rangle_\omega^{\text{ret}}$  is the Fourier-transform of the retarded Green's function of the current operator,  $\langle \langle \hat{I}_{j\sigma} | \hat{I}_{j'\sigma'} \rangle \rangle_t^{\text{ret}} = -i\Theta(t) \langle [\hat{I}_{j\sigma}(t), \hat{I}_{j'\sigma'}(0)] \rangle$  (we set the time units such that  $\hbar \equiv 1$  throughout the paper). In what follows, we shall focus on the properties of the frequency-dependent conductance of the system

$$G_{jj'}^{\sigma\sigma'}(\omega) = \text{Re} \left\{ \mathcal{G}_{jj'}^{\sigma\sigma'}(\omega) \right\} = -\frac{1}{\omega} \text{Im} \left\{ \langle \langle \hat{I}_{j\sigma} | \hat{I}_{j'\sigma'} \rangle \rangle_\omega^{\text{ret}} \right\}. \quad (8)$$

The current operator for our setup is given by

$$\hat{I}_{j\sigma} = ie \left( v_j \hat{\psi}_{j\sigma}^\dagger \hat{d}_\sigma - \text{H.c.} \right) \quad (9)$$

with

$$\hat{\psi}_{j\sigma}^\dagger = \int \sqrt{\rho_j} \hat{c}_{j\epsilon\sigma}^\dagger d\epsilon \quad (10)$$

being the corresponding field operator for the creation of a spin- $\sigma$  electron in the  $j$ -th lead. We introduce an effective tunnel-matrix element,  $v = \sqrt{v_L^2 + v_R^2}$ , and perform a transformation from the *left-right* to the *even-odd* basis

$$\hat{\psi}_\sigma^e = \frac{v_L}{v} \hat{\psi}_{L\sigma} + \frac{v_R}{v} \hat{\psi}_{R\sigma}, \quad (11)$$

$$\hat{\psi}_\sigma^o = -\frac{v_R}{v} \hat{\psi}_{L\sigma} + \frac{v_L}{v} \hat{\psi}_{R\sigma}. \quad (12)$$

Then, for the even (odd) current operator one finds

$$\hat{I}_\sigma^{e(o)} = ive \hat{\mathcal{I}}_\sigma^{e(o)}, \quad (13)$$

with

$$\hat{\mathcal{I}}_\sigma^{e(o)} = \hat{\psi}_\sigma^{e(o)\dagger} \hat{d}_\sigma - \hat{d}_\sigma^\dagger \hat{\psi}_\sigma^{e(o)}, \quad (14)$$

such that  $\hat{I}_{j\sigma}$  can be expressed as

$$\hat{I}_{j\sigma} = ie \left[ \frac{v_j^2}{v} \hat{\mathcal{I}}_\sigma^e + (-1)^{\delta_{j,L}} \frac{v_L v_R}{v} \hat{\mathcal{I}}_\sigma^o \right]. \quad (15)$$

Thanks to  $\langle \langle \hat{\mathcal{I}}_\sigma^e | \hat{\mathcal{I}}_{\sigma'}^o \rangle \rangle = \langle \langle \hat{\mathcal{I}}_\sigma^o | \hat{\mathcal{I}}_{\sigma'}^e \rangle \rangle = 0$ , one obtains

$$\begin{aligned} \frac{G_{jj'}^{\sigma\sigma'}(\omega)}{G_0} &= -\delta_{\sigma\sigma'} \eta_{jj'} \frac{2\Gamma_L \Gamma_R}{\Gamma} \frac{1}{\omega} \text{Im} \left[ \langle \langle \hat{\mathcal{I}}_\sigma^e | \hat{\mathcal{I}}_{\sigma'}^{o\dagger} \rangle \rangle_\omega^{\text{ret}} \right] \\ &\quad - \frac{2\Gamma_j \Gamma_{j'}}{\Gamma} \frac{1}{\omega} \text{Im} \left[ \langle \langle \hat{\mathcal{I}}_\sigma^e | \hat{\mathcal{I}}_{\sigma'}^{e\dagger} \rangle \rangle_\omega^{\text{ret}} \right], \end{aligned} \quad (16)$$

where  $\Gamma = \Gamma_L + \Gamma_R$ ,  $G_0 = 2e^2/h$ , and  $\eta_{jj'} = 1$  if  $j = j'$  and  $\eta_{jj'} = -1$  otherwise.

Note that  $\hat{\psi}_\sigma^o$  is not present in the tunneling Hamiltonian, Eq. (3), *i.e.* it is just a free fermionic field whose Green's functions are known exactly. Thus, one can relate the odd contribution to the quantum dot spectral function through the Wick theorem without introducing any approximations. On the other hand, the current correlation function associated with the even channel needs to be determined explicitly. Then, the formula for the frequency-dependent conductance can be written in a more compact form as [8, 60, 61]

$$\frac{G_{jj'}^{\sigma\sigma'}(\omega)}{G_0} = \delta_{\sigma\sigma'} \eta_{jj'} \frac{2\Gamma_L \Gamma_R}{\Gamma^2} g_\sigma^o(\omega) + \frac{2\Gamma_j \Gamma_{j'}}{\Gamma^2} g_{\sigma\sigma'}^e(\omega) \quad (17)$$

with the functions

$$g_\sigma^o(\omega) = \frac{\Gamma}{2\omega} \int \text{Im} \langle \langle \hat{d}_\sigma | \hat{d}_\sigma^\dagger \rangle \rangle_{\omega'}^{\text{ret}} [f(\omega'+\omega) - f(\omega'-\omega)] d\omega', \quad (18)$$

and

$$g_{\sigma\sigma'}^e(\omega) = -\frac{\Gamma}{\omega} \text{Im} \langle \langle \hat{\mathcal{I}}_\sigma^e | \hat{\mathcal{I}}_{\sigma'}^{e\dagger} \rangle \rangle_\omega^{\text{ret}}, \quad (19)$$

where  $f(\omega) = [1 + \exp(\omega/T)]^{-1}$  is the Fermi-Dirac distribution function ( $k_B \equiv 1$ ).

## C. Treatment of the correlations

To deal with the correlation effects in the low-temperature regime where the Kondo effect emerges, we make use of the NRG approach [56, 62, 63] in its full-density-matrix implementation [64], which allows for sum-rule conserving determination of the spectral functions [65] relevant for our study. This method reliably yields the set of low and high energy eigen-states,

and the Green's functions can be calculated from the Lehmann representation, imposing a broadening with the log-Gaussian kernel [65]. We also use the  $z$ -averaging trick [66] with 8 different values of  $z$ , which allows to avoid over-broadening of spectral functions. This is particularly important for correct calculation of the even contribution, where  $\langle\langle \mathcal{I}_\sigma^e | \mathcal{I}_{\sigma'}^e \rangle\rangle_\omega^{\text{ret}} / \omega$  needs to be obtained at small  $\omega$ , cf. Eq. (19). For specific computations we have chosen the following model parameters: the discretization parameter  $\Lambda = 2$ , the number of states kept per iteration  $N_K = 2048$ , and the broadening width in the range  $0.2 < b < 0.35$ . For values of the physical parameters we take  $U = 0.1D$  and  $\Gamma = U/10$ , which allow for clear presentation of numerical results. These remain qualitatively valid as long as the strong coupling regime is successfully reached, and the relevant energy scales are outlined in the following section. We focus on the zero-temperature case ( $T = 0$ ).

### III. RESPONSE FUNCTIONS AND RELEVANT ENERGY SCALES

As can be seen from the above discussion, the behavior of the  $ac$  conductance is essentially determined by two dimensionless conductances  $g_\sigma^o(\omega)$  and  $g_{\sigma\sigma'}^e(\omega)$ . Therefore, it is of great importance to analyze those functions separately. This will be crucial in understanding different contributions to  $G_{jj'}^{\sigma\sigma'}(\omega)$  as well as

$$G_{jj'}(\omega) = \sum_{\sigma\sigma'} G_{jj'}^{\sigma\sigma'}(\omega) \quad (20)$$

depending on a way how the system is biased.

#### A. Odd response function

We start the discussion from the *odd* dimensionless conductance, cf. Eq. (18), presented in Fig. 2. It describes the contribution from the processes that change sign upon the left-right leads exchange, thus corresponding to the transport through the nanostructure from L to R lead. These processes are governed mainly by the local spectral density of QD, symmetrized through the convolution with the corresponding Fermi functions, cf. Eq. (18). Note that the spin symmetry is broken only by the coupling to spin-polarized TS quantified by  $V_M$ , which determines the spin quantization axis. Therefore,  $g_\uparrow^o(\omega)$  exhibits a hump at  $\omega \sim U$ , a minimum corresponding to Coulomb blockade for  $\omega \lesssim U$  and a peak for frequencies below the Kondo temperature  $T_K$ , here defined through the half-width

$$g_\uparrow^o(\omega = T_K) = 0.5. \quad (21)$$

As long as  $T_K > V_M$ , it is practically independent of  $V_M$ , and therefore the well-known estimation [67] remains

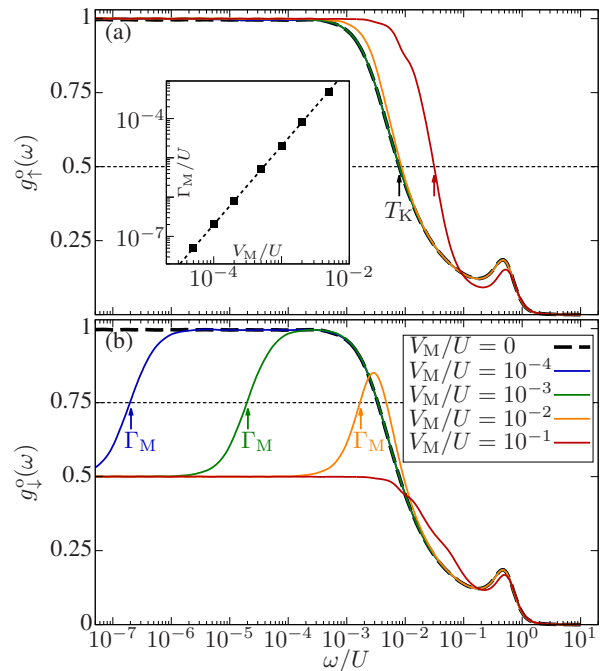


Figure 2. The odd contribution to the  $ac$  conductance  $g_\sigma^o(\omega)$  plotted as a function of frequency for different values of  $V_M$ , as indicated. (a) The spin- $\uparrow$  component, with the  $V_M$ -dependent Kondo scale  $T_K$  indicated with arrows. (b) The spin- $\downarrow$  component, with arrows indicating the relevant  $\Gamma_M$  scale (see the main text for details). Inset shows  $\Gamma_M$  as a function of  $V_M$ , with dashed line corresponding to Eq. (23). The parameters are:  $U = 0.1D$ ,  $\varepsilon_d = -U/2$ ,  $\Gamma = U/10$ , and  $\varepsilon_M = 0$ .

valid,

$$T_K^0 = \sqrt{\frac{U\Gamma}{2}} \exp\left[\frac{\pi \varepsilon_d(\varepsilon_d + U)}{2U\Gamma}\right]. \quad (22)$$

For larger  $V_M$ , however, the results indicate increase of the Kondo scale. Similar tendency has already been reported in earlier numerical studies based on the spectral densities and temperature dependence of the  $dc$  conductance [51, 68, 69], but this goes against intuition concerning a competition between Kondo and Majorana couplings as well as expectations of lack of such dependence from approximate RG schemes [47, 48, 70]. The issue has therefore remained controversial and is fully resolved in favor of  $T_K$  increase only through the analysis of the even contribution to the  $ac$  conductance, see the discussion of Eq. (24) in the sequel.

The other energy scale known from the analysis of conventional spectral functions of Majorana devices is the effective coupling strength to TS [50]

$$\Gamma_M \approx 2V_M^2/\Gamma. \quad (23)$$

It determines the energy scale below which the typical Majorana spectral signatures are visible. Namely, at  $\omega \ll \Gamma_M$  the conductance in spin channel coupled to TS [ $\sigma = \downarrow$ , cf. Fig. 2(b)] is pinned to  $e^2/2h$ . When  $\Gamma_M < T_K$ ,

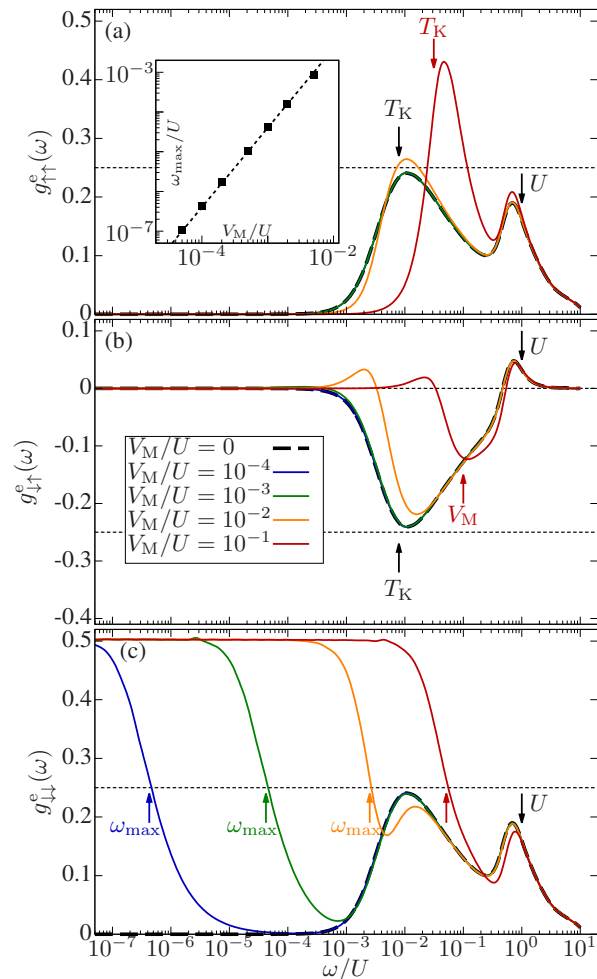


Figure 3. The even contribution to the *ac* conductance  $g_{\sigma\sigma'}^e(\omega)$  plotted as a function of frequency. (a) presents  $g_{\uparrow\uparrow}^e(\omega)$ , (b) shows  $g_{\downarrow\downarrow}^e(\omega) = g_{\uparrow\downarrow}^e(\omega)$ , while (c) displays  $g_{\downarrow\downarrow}^e(\omega)$  calculated for different values of  $V_M$ , as indicated. The arrows indicate the relevant energy scales. Inset shows  $\omega_{\max}$  as a function of  $V_M$ , with dashed line corresponding to  $\omega_{\max} = 2\Gamma_M = 4V_M^2/\Gamma$ . The parameters are the same as in Fig. 2.

the value of  $\Gamma_M$  can be recognized from the condition  $g_{\downarrow}^o(\omega = \Gamma_M) = 0.75$  [71]. Then, the numerical calculations give results in agreement with Eq. (23), cf. the inset in Fig. 2(a).

## B. Even response function

While  $g_{\sigma}^o(\omega)$  provides comparable insight into the system's properties as the local quantum dot spectral density, the *even* contribution,  $g_{\sigma\sigma'}^e(\omega)$ , probes a different Green's function, cf. Eq. (19), and complements the information available from the local spectroscopy. This contribution is even in the left-right leads exchange, so it corresponds to the processes of charging and discharging the quantum dot, and transport from normal leads to the topological superconductor. The two spin indices of

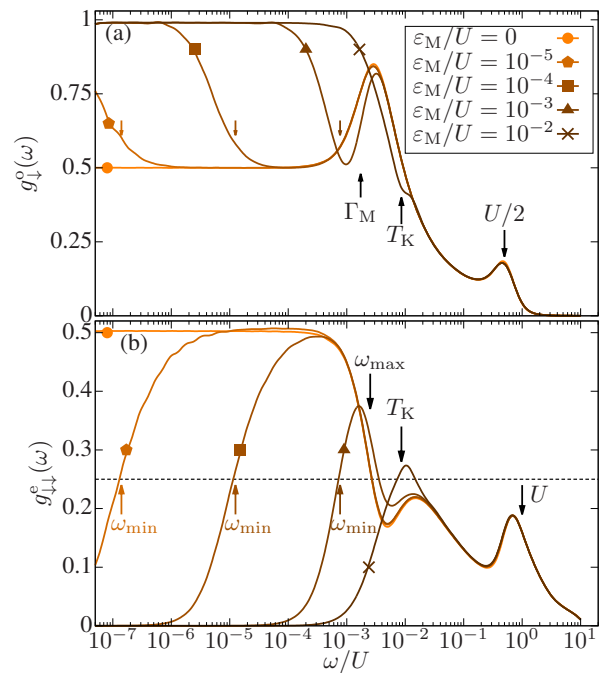


Figure 4. (a) The odd and (b) even contributions to the spin- $\downarrow$  response function due to a spin- $\downarrow$  voltage calculated for  $V_M = 10^{-2}U$  and a few chosen values of  $\epsilon_M$ , as indicated. The other parameters the same as in Fig. 2. The arrows indicate relevant energy scales, with unlabeled arrows in (a) corresponding to relevant  $\omega_{\min}$  shown in (b).

$g^e$  correspond to the response and voltage bias, and the cross-terms appear as a consequence of effective spin exchange interactions induced by Coulomb correlations in the Hamiltonian, Eq. (4). Even though in practice a sum over spins is usually measured, we find it useful to discuss each component separately first. We note that such components could be measured in a double quantum dot setup without the need to resorting to spin-dependent measurements, see Appendix A.

As can be seen in Fig. 3(a),  $g_{\uparrow\uparrow}^e(\omega)$  exhibits a signal characteristic of the Kondo effect, *i.e.* a peak at  $\omega \sim T_K$ , and a second peak for  $\omega \sim U$  [8]. Note that these features do not occur for a resonant model, therefore they are unique signatures of Coulomb interactions and the resulting Kondo effect. Similarly as in Fig. 2(a), one observes now an increase of  $T_K$  with  $V_M$ . This enhancement of  $T_K$  persists even if the wire is not long enough to make the Majorana overlap  $\epsilon_M$  negligible, see Fig. 4, and is most clearly shown in Fig. 5(a). For different values of  $V_M$ , from our numerical data we find approximately

$$T_K \approx \sqrt{(T_K^0)^2 + 0.1V_M^2}, \quad (24)$$

which remains valid when the TS wire is short,  $\epsilon_M \neq 0$ , cf. Fig. 4(a) and Fig. 5(a).

In Fig. 3(b) the opposite-spin-response is shown [note that  $g_{\uparrow\downarrow}^e(\omega) = g_{\downarrow\uparrow}^e(\omega)$  follows from the definition of relevant Green's functions, cf. Eq. (19), and the bosonic

character of current operators]. Already for  $V_M = 0$ , it possesses a set of unique features [9]. It exhibits a positive peak for  $\omega \sim U$  and a negative one at  $\omega \sim T_K$ . This negative sign means that for the corresponding frequencies the voltage in spin channel  $\sigma$  induces a negative current in the other spin channel, which could be seen as a consequence of the Kondo singlet oscillations. When a spin- $\uparrow$  electron leaves the quantum dot, its singlet companion secures single-occupancy of the dot. This is further confirmed by the fact that for  $V_M = 0$  the negative peak of  $g_{\sigma\uparrow}^e(\omega)$  is a mirror-image of the corresponding positive peak in  $g_{\sigma\sigma}^e(\omega)$ , visible in Figs. 3(a) and (c); see also the discussion of Fig. 7. This means that the charge current in one spin channel is compensated by the opposite current of the other spin channel, which is the essence of an antiferromagnetic spin exchange. When  $\omega \sim T_K$ , the spin exchange is almost in resonance with the driving frequency, leading to fractional value of the components of the even conductance,  $\eta_{\sigma\sigma'} g_{\sigma\sigma'}^e = 1/4$  and the unitary value of the spin conductance.<sup>1</sup> When  $\omega$  significantly exceeds  $T_K$ , the process becomes inefficient, as spin exchange no longer keeps up to rapidly oscillating driving bias.

For  $0 < V_M \leq 10^{-2}U$ , the picture changes mainly quantitatively: the negative peak position shifts toward higher  $\omega$  as a consequence of increase of  $T_K$ . However, it should be noted that for  $V_M \gtrsim T_K$ , while the peak in  $g_{\uparrow\uparrow}^e(\omega)$  becomes higher in the presence of TS, the negative peak in  $g_{\downarrow\uparrow}^e(\omega)$  is reduced and supplemented with a small positive one at lower  $\omega$ ; cf. the curves for  $V_M = 10^{-2}$  in Fig. 3(a-b). This could be understood as the competition between the Kondo exchange and Andreev processes, the latter ones relevant here only for the spin-down electrons. It becomes even more apparent for larger  $V_M$ ,  $V_M \gtrsim T_K^0$ , when the positions of the peaks become different: in  $g_{\uparrow\uparrow}^e(\omega)$  the peak remains at  $T_K(V_M)$ , while in  $g_{\downarrow\uparrow}^e(\omega)$  it follows simply  $V_M$  [cf. the curve for  $V_M = 10^{-1}U$  in Fig. 3(a)], which is the energy scale of the QD-TS hopping. This leads to  $g_{\uparrow\uparrow}^e(\omega \approx V_M) < -g_{\downarrow\uparrow}^e(\omega \approx V_M)$ , and thus one obtains a *negative* total response in the spin-down channel, cf. Fig. 7.

The most prominent result for the even response function is presented in Fig. 3(c), which shows the spin- $\downarrow$  response to the spin- $\downarrow$  bias, i.e.  $g_{\downarrow\downarrow}^e(\omega)$ . Besides the Kondo-related peak identical to the one visible in  $g_{\uparrow\uparrow}^e(\omega)$ ,  $g_{\downarrow\downarrow}^e(\omega)$  acquires a non-zero value in the static limit ( $\omega \rightarrow 0$ ). This means steady current flowing into QD at a con-

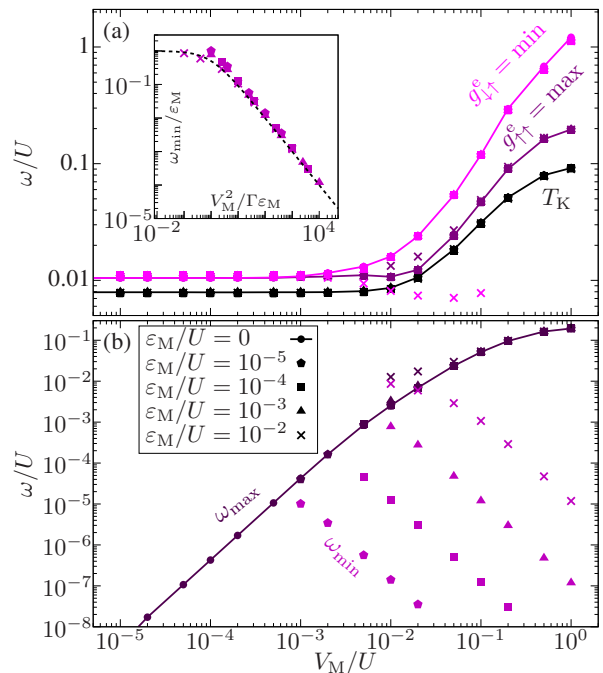


Figure 5. (a) The Kondo scale  $T_K$ , defined in Eq. (21), estimation of the Kondo scale determined as the position of the maximum in  $g_{\uparrow\uparrow}^e(\omega)$ , and the position of the minimum in  $g_{\downarrow\uparrow}^e(\omega)$ , as functions of  $V_M$ . (b)  $\omega_{\max}$  and  $\omega_{\min}$  as functions of  $V_M$ . In both panels, lines correspond to  $\varepsilon_M = 0$ , while different point styles correspond to different values of  $\varepsilon_M$ , as indicated. Inset in (a) shows  $\omega_{\min}$  for all considered  $\varepsilon_M$ , appropriately scaled, such that they all collapse to a single curve estimated by Eq. (25) and indicated with a dashed line.

stant bias and can be understood as the current flowing into TS. This result extends to higher  $\omega$ , in fact to  $\omega \sim \omega_{\max} = 2\Gamma_M \approx 4V_M^2/\Gamma$ , as indicated in Fig. 3(c) with upward arrows. The magnitude of  $\omega_{\max}$  is further analyzed in Fig. 5(b).

### C. Role of Majorana overlap

The topological superconducting nanowires should be sufficiently long in order to prevent any overlap between the Majorana zero-energy modes. In practice, however, this may be difficult to achieve and a non-negligible  $\varepsilon_M$  may exist, as assumed in Eq. (4). This quite drastically changes the situation, because the Kondo-Majorana fixed point is not stable against such perturbation, *i.e.*  $\varepsilon_M$  is a *relevant* perturbation in the RG sense. Still, the latter determines the physics at the intermediate temperatures  $T$ , namely when  $|\varepsilon_M| < T < T_K$  [49]. This looks similar for the *ac* response, where  $\omega$  plays the role of  $T$ , as is shown in Fig. 4. In both  $g_{\downarrow}^o(\omega)$  and  $g_{\downarrow\downarrow}^e(\omega)$  there appears a scale, denoted here as  $\omega_{\min}$ , whose magnitude can be estimated from

$$\omega_{\min} = \varepsilon_M(1 + \Gamma_M/\varepsilon_M)^{-1}. \quad (25)$$

<sup>1</sup> To see that this is indeed the value relevant in the unitary regime, let us assume that the corresponding  $\omega$ -dependent spin bias  $V_{j\uparrow}(\omega) = -V_{j\downarrow}(\omega) = V^e(\omega)/2$  is applied to both normal leads. Then, the charge currents fulfill,  $I_{j\sigma}(\omega) = (G_0/2)V^e(\omega)[g_{\sigma\uparrow}^e(\omega) - g_{\sigma\downarrow}^e(\omega)]$ , and the total spin current from normal electrodes is  $I_S(\omega) = \sum_{j\sigma} \sigma I_{j\sigma}(\omega) = G_0V^e(\omega)[g_{\uparrow\uparrow}^e(\omega) - g_{\uparrow\downarrow}^e(\omega) - g_{\downarrow\uparrow}^e(\omega) + g_{\downarrow\downarrow}^e(\omega)]$ . Consequently,  $I_S(\omega)$  becomes  $G_0V^e$  at resonance, i.e. for  $\omega \approx T_K$ , which is indeed the unitary value.

This is simply the energy scale related to crossing to a stable fixed point, which for  $\varepsilon_M \neq 0$  is not the Majorana-Kondo but rather the conventional Kondo fixed point.

As a summary of this section, all the relevant energy scales are plotted in Fig. 5. In panel (a) it is shown that  $\varepsilon_M$  does not really influence  $T_K$  and only for  $\varepsilon_M \sim V_M$  it may affect the position of  $g_{\downarrow\uparrow}^e(\omega)$  minimum. On the other hand, panel (b) presents how the range of Majorana regime in the  $ac$  response, in particular  $\omega_{\min}(V_M, \varepsilon_M)$ , changes with  $V_M$  for different  $\varepsilon_M$ . The universality of the formula (25) is demonstrated in the inset of Fig. 5(a).

#### IV. AC CONDUCTANCE IN DIFFERENT BIAS CONFIGURATIONS

Having discussed the odd and even response functions, let us now examine the characteristics of the frequency-dependent conductance for three different bias configurations. In the first one, referred to as antisymmetric bias configuration, the voltage is applied as,  $-V_{L\sigma}(\omega) = V_{R\sigma}(\omega) \equiv V^o(\omega)/2$ . Then, assuming symmetrical coupling of the quantum dot to the leads,  $\Gamma_L = \Gamma_R$ , we have

$$-I_{L\sigma}(\omega) = I_{R\sigma}(\omega) = G_\sigma^o(\omega)V^o(\omega), \quad (26)$$

with the  $ac$  conductance given only by the odd response function

$$G_\sigma^o(\omega) = \frac{G_0}{2}g_\sigma^o(\omega). \quad (27)$$

This is in contrast to the symmetric bias configuration,  $V_{L\sigma}(\omega) = V_{R\sigma}(\omega) \equiv V^e(\omega)$  in which one can probe the even contribution to the frequency-dependent conductance. In this case, the total  $ac$  current entering the quantum dot from the normal leads can be written as

$$I_{L\sigma}(\omega) + I_{R\sigma}(\omega) = G_\sigma^e(\omega)V^e(\omega), \quad (28)$$

with the conductance in spin  $\sigma$  channel

$$G_\sigma^e(\omega) = \sum_{jj'\sigma'} G_{jj'\sigma'}^{\sigma\sigma'} = 2G_0 [g_{\sigma\uparrow}^e(\omega) + g_{\sigma\downarrow}^e(\omega)]. \quad (29)$$

In general, for  $\Gamma_L = \Gamma_R$ , any spin-independent voltage bias  $V_{j\uparrow}(\omega) = V_{j\downarrow}(\omega) = V_j(\omega)$  can be decomposed into the even and odd parts. Still, we find it useful to discuss also the case when the time-dependent voltage is applied to one lead, i.e.  $V_R = 0$ . One then has

$$I_{j\sigma}(\omega) = G_\sigma^{jL}(\omega)V_L(\omega) \quad (30)$$

with

$$G_\sigma^{LL}(\omega) = \frac{G_0}{2} [g_{\sigma\uparrow}^e(\omega) + g_{\sigma\downarrow}^e(\omega) + g_\sigma^o(\omega)], \quad (31)$$

$$G_\sigma^{RL}(\omega) = -\frac{G_0}{2} [g_{\sigma\uparrow}^e(\omega) + g_{\sigma\downarrow}^e(\omega) - g_\sigma^o(\omega)] \quad (32)$$

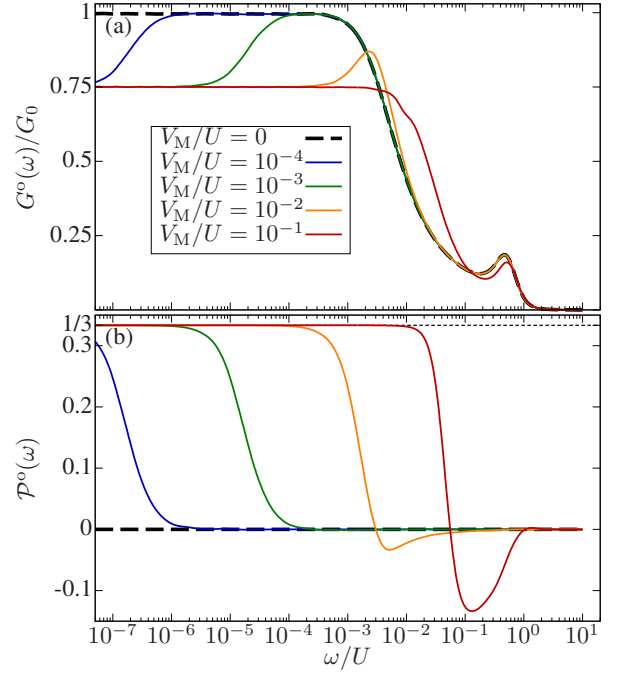


Figure 6. (a) The total conductance between the normal leads and (b) its spin polarization calculated as function of  $\omega$  assuming small spin-independent bias applied antisymmetrically to the left and right leads. The parameters are the same as in Fig. 2.

and the minus sign in Eq. (32) follows from taking the current from the quantum dot to the right lead as positive.

In the static limit,  $\omega \rightarrow 0$ , the net current flowing from the normal leads to the dot must drain into the superconducting nanowire. In contrast, for  $\omega \neq 0$ , the processes of charging and discharging can yield non-zero signal. Note that we assume here the superconductor to be always grounded, *i.e.* no bias is ever applied to it.

In the following, we discuss the total conductances  $G^x(\omega) = G_\uparrow^x(\omega) + G_\downarrow^x(\omega)$  and the corresponding spin polarization, given by

$$\mathcal{P}^x(\omega) = \frac{|G_\uparrow^x(\omega)| - |G_\downarrow^x(\omega)|}{|G_\uparrow^x(\omega)| + |G_\downarrow^x(\omega)|}, \quad (33)$$

where  $x$  is one of the labels  $\{e, o, LL, LR\}$ , instead of addressing each spin component separately. It should be noted that in our model we do not include any magnetic field acting on the QD, so only the hopping to TS determines the spin quantization axis. This might be relevant for TS nanowires achieved through deposition of magnetic adatoms on the ferromagnetic substrate. It may be also relevant for more conventional semiconductor-based wires, assuming the correspondingly different  $g$ -factor for the quantum dot.

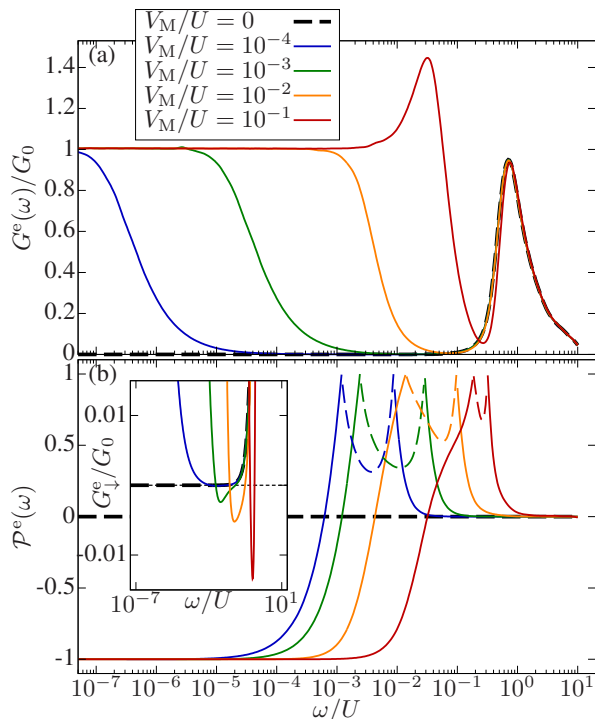


Figure 7. (a) Total conductance between the leads and quantum dot and (b) the corresponding spin polarization calculated as function of  $\omega$ . The dashed lines in (b) were used to indicate the range of  $\omega$  where  $G^e(\omega) < 0$ . The inset shows  $G^e_{\downarrow}(\omega)$  in this regime. The parameters are as in Fig. 3, with identical small spin-independent bias applied to both left and right leads,  $V_{L\sigma}(\omega) = V_{R\sigma}(\omega) = V^e(\omega)$ .

### A. The case of antisymmetric biasing

Let us start with the situation when an antisymmetric bias is applied to the system, *i.e.*  $-V_{L\sigma}(\omega) = V_{R\sigma}(\omega) = V^o(\omega)/2$ . In such a case, according to Eq. (27), each spin component of the conductance is basically given by  $g^o_{\sigma}(\omega)$ , such that  $G(\omega) \equiv G^o(\omega) = \sum_{\sigma} G^o_{\sigma}(\omega)$ . While the behavior of  $g^o_{\sigma}(\omega)$  has been discussed in the context of Fig. 2, here we focus on the total *ac* conductance and its spin polarization, which are presented in Fig. 6. First of all, one can see that the zero-frequency total conductance  $G^o(\omega = 0) = 3e^2/2h = (3/4)G_0$  for  $V_M \neq 0$ , cf. Fig. 6(a). The order of magnitude of  $\omega_{\max}$  can be roughly estimated as the energy scale where this value is reached.

Any non-zero  $V_M$  leads to spin imbalance, also at  $\omega = 0$ , where  $g^o_{\uparrow}(0) = 2g^o_{\downarrow}(0)$ . This leads to  $\mathcal{P}^o(\omega \ll \omega_{\max}) = 1/3$ , as is visible in Fig. 6(b). On the other hand, whenever  $V_M \gtrsim T_K$ , at  $\omega \sim V_M$ , the spin- $\downarrow$  conductance is enhanced in comparison to the spin- $\uparrow$  one, due to additional TS-QD processes possible in this spin channel. Consequently,  $\mathcal{P}$  becomes negative in this range of frequencies.

### B. The case of symmetric biasing

In turn, we focus on the case of symmetric biasing, that is, we assume  $V_{L\sigma}(\omega) = V_{R\sigma}(\omega) = V^e(\omega)$  and define the conductance through the total current entering the quantum dot from both normal leads. Note that in this biasing situation, the total conductance is given by the even contribution only, *i.e.*  $G(\omega) \equiv G^e(\omega) = \sum_{\sigma} G^e_{\sigma}(\omega)$ . The corresponding conductance is displayed in Fig. 7(a). First of all, it exhibits a large peak at frequencies of the order of Coulomb interaction strength  $U$ , irrespective of  $V_M$ . This signal is a signature of charging-discharging dynamics, and remains the only feature relevant for  $V_M = 0$  case, *i.e.* when QD is decoupled from TS. For  $V_M > 0$ , however, the most prominent feature is a low-frequency ( $\omega \lesssim \omega_{\max}$ ) plateau of perfectly spin-polarized conductance  $2e^2/h$ , cf. the latter plotted in Fig. 7(b). This is a signature of resonant Andreev transport through QD into the TS [40, 72, 73], persisting at finite frequencies. Ultimately, for  $V_M \gtrsim T_K$  (see the curve for  $V_M = 10^{-1}U$  in the figure) an additional peak at  $\omega \sim T_K$  is present. This is a consequence of separation between positions of positive peak in  $g^e_{\uparrow}(\omega)$ , present always at  $\omega \sim T_K$ , and negative peak in  $g^e_{\downarrow}(\omega)$ , shifting from  $\omega \sim T_K$  for  $V_M \lesssim T_K$  toward  $\omega \sim V_M$  for  $V_M \gtrsim T_K$ ; see also the discussion of Fig. 3. This additional peak increases the total dynamical conductance over  $G_0$  threshold and partially lifts the spin polarization around  $\omega \sim T_K$ .

As has been pointed out in the context of Fig. 3, already for  $0 < V_M \lesssim T_K$ , the compensation between  $\omega \sim T_K$  peaks of  $g^e_{\uparrow}(\omega)$  and  $g^e_{\downarrow}(\omega)$  becomes imperfect. While this is barely visible in the conductance curves, which show almost completely suppressed transport, the plot of spin polarization, Fig. 7(b), reveals vast domination of the spin- $\uparrow$  channel transport. At two frequencies, the spin- $\downarrow$  contribution vanishes, and  $\mathcal{P}^e(\omega) = 1$ . Between these frequencies  $G^e_{\downarrow}(\omega)$  even becomes genuinely negative, *i.e.* the spin- $\downarrow$  current flows in opposite direction than the spin- $\uparrow$  one. This means a conversion of a conventional bias to the spin current, which might be interesting from the point of view of applications.

### C. The case of one-lead pumping

Finally, as an example of a general situation, where both odd and even channels are present, we consider *ac* bias applied to only one (left) lead. The conductance between this lead and the quantum dot is given by Eq. (31) and presented in Fig. 8(a) for selected values of  $V_M$ . Clearly, it interpolates between  $G^o(\omega)$  and  $G^e(\omega)$ , cf. Fig. 6 and Fig. 7. It exhibits a peak at  $\omega \sim U$  and grows to approximately  $2e^2/h$  for  $\omega \lesssim T_K$ . Quite unfortunately, most of the Majorana features get washed away, as a consequence of the compensation between  $G^e(\omega)$  increase and  $G^o(\omega)$  suppression with increasing  $V_M$ . The only remaining features are small bumps appearing at frequencies  $\omega \sim \omega_{\max}$ . Similar is the fate of the spin po-



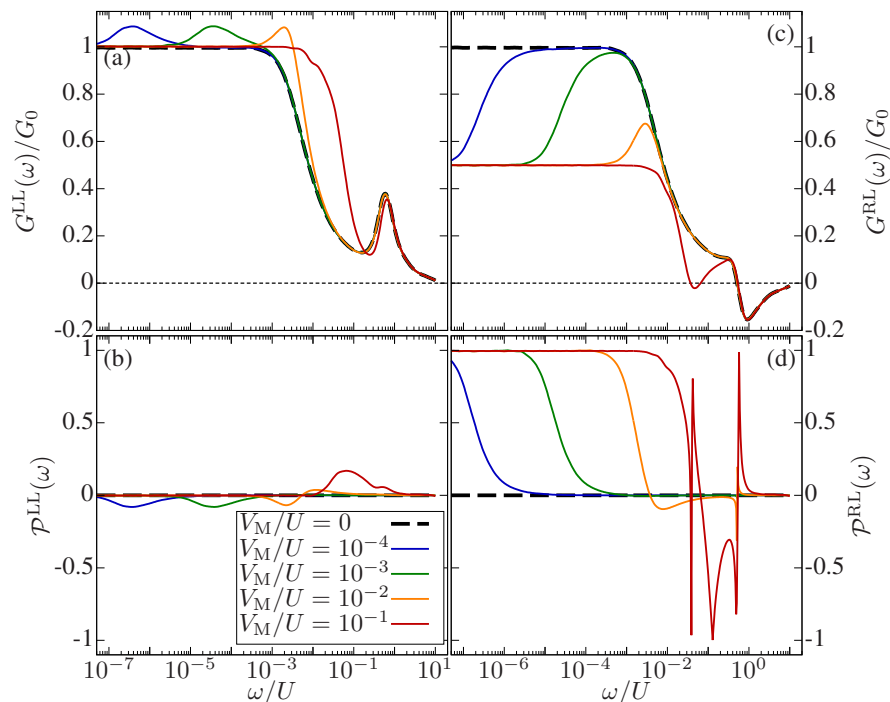


Figure 8. (a) The dynamical conductance from the left lead to the quantum dot and (b) the corresponding spin polarization, as well as (c) the conductance from the right lead to the quantum dot together with (d) its spin polarization. The parameters are the same as in Fig. 2, with a time-dependent voltage applied to the left lead only.

larization features, presented in Fig. 8(b), where only a relatively low signal persists in this range.

Much more interesting features, giving somewhat more insight into the system behavior, are revealed in the response in the other lead, which is proportional to  $G^{\text{RL}}(\omega)$ , cf. Eq. (32). The corresponding conductance is presented in Fig. 8(c). Now, one can see that at  $\omega \lesssim \omega_{\text{max}}$  the system works as an excellent spin filter. The electrons with both spins are pumped between the left lead and the dot. On the other hand, topological superconductor allows only the spin- $\downarrow$  channel to enter, meanwhile the unbiased right lead constitutes a drain for spin- $\uparrow$  channel. At higher  $\omega$ ,  $G^{\text{RL}}(\omega)$  drops below 0. This behavior is easiest to understand for  $\omega \sim U$ , when the processes of charging-discharging the quantum dot are the most effective means of transport, and while most of the charge is supplied by the biased lead, some part is also drawn from the other normal lead. Additionally, when the peaks in  $g_{\uparrow\uparrow}^e(\omega)$  and  $g_{\uparrow\downarrow}^e(\omega)$  are separated (see the curves corresponding to  $V_M = 10^{-1}U$  in Fig. 8), a complex interplay between all different contributions gives rise to an additional dip of the conductance visible in Fig. 8(c) and violent changes of  $\mathcal{P}^{\text{RL}}(\omega)$  around the zeros of conductances in both spin channels, see Fig. 8(d). Such sharp frequency-driven changes of the sign of spin polarization might be very useful for applications.

## V. DISCUSSION

In this section, we point out possible extensions and limitations of our considerations, discuss other treatments using effective Hamiltonians and comment on the influence of disorder on Majorana quasiparticle features.

Correlation effects driven by the Coulomb repulsion between opposite-spin electrons on an Anderson-type impurity can be described under certain conditions within effective spin models, determining the exchange coupling perturbatively by canonical transformation [74]. This approach proved to be successful when applied to nanostructures with a correlated quantum dot placed between metallic lead and conventional superconductor, clarifying the subtle relationship of the proximity-induced electron pairing and the Kondo physics [75]. Effective spin interactions of the Anderson impurity side-attached to the topological superconducting nanowire have been also investigated in this perturbative framework [47, 48, 70]. Such study revealed that the Majorana mode affects the spin-exchange potential and additionally introduces the Zeeman field, lifting the spin degeneracy of quantum dot energy level. In consequence, the spin-resolved Kondo effect of the quantum dot is profoundly altered [50]. However, perturbative elimination of charge fluctuations at QD can be applied only when all Hamiltonian terms changing QD occupation [*i.e.*  $\Gamma$  and  $V_M$ , cf. Eq. (3) and Eq. (4)] are indeed irrelevant, while the exchange interactions scale toward strong coupling fixed point. There-

fore, without RG analysis including charge fluctuation terms, validity of such effective low-energy spin model is limited. Here, we have avoided this difficulty simply by taking charge fluctuations into account, which does not constitute any significant complication within the proposed computation scheme.

A possible route for treating the nonequilibrium effects induced by a periodically varying voltage applied across the quantum dot would be the time-dependent Schrieffer-Wolff transformation. Such approach adopted to the correlated quantum impurity placed between two normal leads displayed the two-channel Kondo physics [76], where impurity is screened by separate conduction bands, corresponding to parity-even and odd superpositions of the external leads. Upon varying the amplitude and frequency of a drive, the system can be tuned to the critical point with symmetric coupling of the impurity to both channels. Approaching this critical point, the spin susceptibility increases logarithmically with time. In the regime where energy absorption is low, the time-evolution of the impurity spin indeed revealed dynamics typical for the two-channel model [76]. This treatment is perturbative, so its validity beyond weak coupling regime is not clear.

More generally, joint influence of the strong correlations and periodic driving can be investigated from the perspective of the Floquet theory, which can be regarded as time-equivalent of the spatial Bloch treatment. Using such an approach to the setup with the Kondo impurity embedded between two metallic leads, a coherent dressing of the driving field manifested by side replicas of the Kondo resonance of the averaged conductance has been predicted [77]. Main virtue of this method is its applicability from the weak to strong driving and ability to deal with short voltage pulses. The Floquet-Kondo engineering enables also derivation of the effective models with multichannel degenerate points (even though the starting Hamiltonian is a single channel one) [78]. The emergent channels of various physical situations in presence of *ac* external fields can be controlled by changing e.g. polarization, frequency, and/or amplitude. The resulting multichannel Kondo models could host a plethora of exotic phenomena, including non-Abelian anyons [78] and novel types of nonequilibrium superconductivity [79]. The Floquet-formalism picture of the Kondo-Majorana interplay would be a significant extension of the results discussed here, in principle lifting the characteristic Kubo formalism assumption of weak driving. However, it would require equally significant development of the methodology to address such a complex, periodically driven, strongly correlated system without introducing uncontrolled (*e.g.* perturbative) approximations.

The boundary modes harbored in topological phases should be immune to disorder, although in particular setups this situation can vary. For instance, disorder might play an important role by inducing local features resembling the topological boundary states. For this reason, additional checks, *e.g.* by inspecting the behavior of the

*ac*-conductance, could resolve the true nature of the zero-energy quasiparticles. In particular, robustness of the Majorana modes of the inhomogeneous Rashba nanowire deposited on superconducting substrate has been discussed in Ref. [80] (see also other papers cited therein). It seems, however, that magnetic field (magnetic moments) would be useful because it induces a splitting of the trivial bound states, while the Majorana mode stays robust at zero energy. Thus, in a regime of the magnetic field corresponding to the topologically nontrivial superconductivity, there is some possibility to discriminate between the Majorana and disorder-induced quasiparticles.

## VI. CONCLUSIONS AND OUTLOOK

We have investigated the dynamical charge transport through the correlated quantum dot side-attached to the topological superconducting nanowire, focusing on the strong coupling regime. We have identified the frequency range where the signatures of Majorana modes occupying the ends of the wire can be observed. Our analysis of all the contributions to conductance between the normal leads and the quantum dot revealed that in general total conductance is a combination of two contributions: the odd and even in exchanging the left and right leads, respectively. We have proposed several biasing schemes allowing for addressing each of these contributions separately, and we also discussed the case of driving only one of the normal leads when both contributions are relevant.

We have shown that at low frequencies the even contribution remains non-zero, leading to generalization of the zero-bias anomaly known from *dc* studies to the *ac* case. At higher frequencies clear signatures of the Coulomb interactions and the Kondo effect are reported. When properly tuned, the device can be used to generate the spin current (with much smaller charge current still present) and fully spin-polarized electric current. The full frequency dependence uniquely characterizes the relevant low-temperature Kondo-Majorana interplay, which we hope will stimulate and foster further endeavors to observe it experimentally.

For experimental verification of our predictions we propose to use the quantum dot-Majorana mode hybrid structures, either based on semiconducting nanowires [81] or self-organized magnetic chains (for instance Fe atoms) deposited on superconducting surface with side attached quantum impurities which can be crafted atom-by-atom [82]. In the first case, the experimental spectroscopy would rely on measurement of *ac* ballistic tunneling conductance, whereas in the second situation the relevant measurements could be done with periodically modulated scanning tunneling spectroscopy. Using microwave spectroscopy one could also detect nonequilibrium signatures of the Andreev-Majorana bound states [83]. In all cases, the probed frequencies should be safely inside the topological gap (fractions of meV).

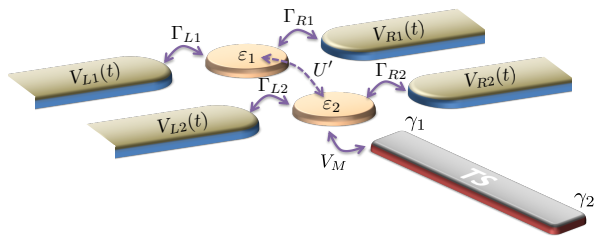


Figure 9. Schematic for alternative realization of the system based on a double quantum dot setup.

## ACKNOWLEDGMENTS

This research project has been supported by the National Science Centre (Poland) through Grant No. 2018/29/B/ST3/00937. T.D. and I.W. also acknowledge National Science Centre (Poland) Grant No. 2022/04/Y/ST3/00061.

### Appendix A: Alternative experimental realization

As we have shown in the main text of the paper, application of the symmetric or antisymmetric voltage bias between the leads may be used to address the chosen response function summed over source spins. However, even if spin-sensitive measurements are performed, the even contribution is always a sum of two terms, cf. Eq. (29). Separately addressing one of them would require application of the bias to only one spin species in the normal leads, which can pose a considerable experimental challenge. However, an alternative system might be proposed, where  $g_{\sigma\bar{\sigma}}^e(\omega)$  would not require such a sophisticated biasing, at the expense of adding one more quantum dot to the system, as depicted in Fig. 9. The device presented there has the same low energy struc-

ture, when one assumes that quantum dots are very small (thus the corresponding  $U$  is very large) and are placed in a strong magnetic field, rendering one of the spins (say spin- $\uparrow$ ) irrelevant for the low-energy processes. Proximity of quantum dots enforces also inter-dot Coulomb repulsion  $U'$ , and we assume that the direct hopping between the dots is suppressed. In such a scenario, the spin becomes irrelevant, while the quantum dot index plays the role of an isospin. Only the second dot is directly coupled to the topological superconductor, and each quantum dot has its own bath of free electrons in leads 1 and 2, correspondingly. Together they constitute a single effective electrode possessing the isospin index, and  $U'$  leads to Coulomb blockade and the (isospin) Kondo effect when the two QDs are (in total) singly occupied. Crucially, now the bias applied to only one (iso)spin channel is easily realizable, simply as a bias applied only to leads connected to the relevant quantum dot, and the response can also be measured in each of these separately.

### Appendix B: The case of conventional superconductor

One of the most prominent results of our study is that the even contribution to the frequency-dependent conductance maintains the universal value of  $G_0$  over an extended range of frequencies. Here we would like to stress, that while the existence of non-zero conductance at low  $\omega$  is a result of superconductivity, its universal character is a clear hallmark of a topological protection. Namely, we have verified through direct calculations that when the TS is replaced by a conventional superconductor,  $G^e(\omega \rightarrow 0) > 0$ , but is not universal. Its magnitude becomes significant only for the quantum dot-superconductor coupling strength  $\Gamma_S$  exceeding  $\sim U/4$ . Therefore, any effect stemming from direct coupling of the dot to the superconducting shell, covering the nanowire in typical realizations of TS, can be safely ignored.

- 
- [1] Ya. M. Blanter and M. Büttiker, Shot noise in mesoscopic conductors, *Phys. Rep.* **336**, 1 (2000).
  - [2] C. P. Moca, C. Mora, I. Weymann, and G. Zaránd, Noise of a Chargeless Fermi Liquid, *Phys. Rev. Lett.* **120**, 016803 (2018).
  - [3] G. Michałek, B. R. Bulka, T. Domański, and K. I. Wysokiński, Statistical correlations of currents flowing through a proximized quantum dot, *Phys. Rev. B* **101**, 235402 (2020).
  - [4] S. A. González, L. Melischek, O. Peters, K. Flensberg, K. J. Franke, and F. von Oppen, Photon-assisted resonant Andreev reflections: Yu-Shiba-Rusinov and Majorana states, *Phys. Rev. B* **102**, 045413 (2020).
  - [5] J. Siegl, J. Picó-Cortés, and M. Grifoni, Particle conserving approach to ac-dc driven interacting quantum dots with superconducting leads, *Phys. Rev. B* **107**, 115405 (2023).
  - [6] T.-K. Ng, ac Response in the Nonequilibrium Anderson Impurity Model, *Phys. Rev. Lett.* **76**, 487 (1996).
  - [7] R. López, R. Aguado, G. Platero, and C. Tejedor, Kondo Effect in ac Transport through Quantum Dots, *Phys. Rev. Lett.* **81**, 4688 (1998).
  - [8] C. P. Moca, I. Weymann, and G. Zaránd, Theory of frequency-dependent spin current noise through correlated quantum dots, *Phys. Rev. B* **81**, 241305(R) (2010).
  - [9] C. P. Moca, I. Weymann, and G. Zarand, Theory of ac spin current noise and spin conductance through a quantum dot in the Kondo regime: Equilibrium case, *Phys. Rev. B* **84**, 235441 (2011).
  - [10] A. Crépieux, S. Sahoo, T. Q. Duong, R. Zamoum, and M. Lavagna, Emission Noise in an Interacting Quantum Dot: Role of Inelastic Scattering and Asymmetric Coupling to the Reservoirs, *Phys. Rev. Lett.* **120**, 107702 (2018).

- [11] G. Stefanucci and S. Kurth, AC transport in correlated quantum dots: From Kondo to Coulomb blockade regime, *Phys. Rev. B* **97**, 245415 (2018).
- [12] Y. Wang, C. Setty, S. Sur, L. Chen, S. Paschen, D. Natelson, and Q. Si, Shot noise as a characterization of strongly correlated metals, arXiv 10.48550/arXiv.2211.11735 (2022), 2211.11735.
- [13] T. V. Shahbazyan, I. E. Perakis, and M. E. Raikh, Spin Correlations in Nonlinear Optical Response: Light-Induced Kondo Effect, *Phys. Rev. Lett.* **84**, 5896 (2000).
- [14] A. Hijano, F. S. Bergeret, F. Giazotto, and A. Braggio, Microwave-assisted thermoelectricity in  $S$ - $I$ - $S'$  tunnel junctions, *Phys. Rev. Appl.* **19**, 044024 (2023).
- [15] M. Lee, R. López, M.-S. Choi, T. Jonckheere, and T. Martin, Effect of many-body correlations on mesoscopic charge relaxation, *Phys. Rev. B* **83**, 201304(R) (2011).
- [16] G.-W. Deng, L. Henriët, D. Wei, S.-X. Li, H.-O. Li, G. Cao, M. Xiao, G.-C. Guo, M. Schiró, K. Le Hur, and G.-P. Guo, Kondo induced  $\pi$ -phase shift of microwave photons in a circuit quantum electrodynamics architecture, *Phys. Rev. B* **104**, 125407 (2021).
- [17] A. Blais, A. L. Grimsmo, S. M. Girvin, and A. Wallraff, Circuit quantum electrodynamics, *Rev. Mod. Phys.* **93**, 025005 (2021).
- [18] B. R. Bulka, Cooper pair splitter in a photonic cavity: Detection of Andreev scatterings, *Phys. Rev. B* **106**, 085424 (2022).
- [19] G. Platero and R. Aguado, Photon-assisted transport in semiconductor nanostructures, *Phys. Rep.* **395**, 1 (2004).
- [20] G. Zaránd, L. Borda, J. von Delft, and N. Andrei, Theory of Inelastic Scattering from Magnetic Impurities, *Phys. Rev. Lett.* **93**, 107204 (2004).
- [21] L. Borda, L. Fritz, N. Andrei, and G. Zaránd, Theory of inelastic scattering from quantum impurities, *Phys. Rev. B* **75**, 235112 (2007).
- [22] J. Basset, A. Yu. Kasumov, C. P. Moca, G. Zaránd, P. Simon, H. Bouchiat, and R. Deblock, Measurement of Quantum Noise in a Carbon Nanotube Quantum Dot in the Kondo Regime, *Phys. Rev. Lett.* **108**, 046802 (2012).
- [23] B. Hemingway, S. Herbert, M. Melloch, and A. Kogan, Dynamic response of a spin- $\frac{1}{2}$  Kondo singlet, *Phys. Rev. B* **90**, 125151 (2014).
- [24] P. Kot, R. Drost, M. Uhl, J. Ankerhold, J. C. Cuevas, and C. R. Ast, Microwave-assisted tunneling and interference effects in superconducting junctions under fast driving signals, *Phys. Rev. B* **101**, 134507 (2020).
- [25] D. Watfa, R. Delagrè, A. Kadlecová, M. Ferrier, A. Kasumov, H. Bouchiat, and R. Deblock, Collapse of the Josephson emission in a carbon nanotube junction in the kondo regime, *Phys. Rev. Lett.* **126**, 126801 (2021).
- [26] I. Tamir, V. Caspari, D. Rolf, C. Lotze, and K. J. Franke, Shot-noise measurements of single-atom junctions using a scanning tunneling microscope, *Rev. Sci. Instrum.* **93**, 023702 (2022).
- [27] D. E. Liu, M. Cheng, and R. M. Lutchyn, Probing Majorana physics in quantum-dot shot-noise experiments, *Phys. Rev. B* **91**, 081405(R) (2015).
- [28] T. Jonckheere, J. Rech, A. Zazunov, R. Egger, A. L. Yeyati, and T. Martin, Giant shot noise from Majorana zero modes in topological trijunctions, *Phys. Rev. Lett.* **122**, 097003 (2019).
- [29] V. Perrin, M. Civelli, and P. Simon, Identifying Majorana bound states by tunneling shot-noise tomography, *Phys. Rev. B* **104**, L121406 (2021).
- [30] S. Smirnov, Revealing universal Majorana fractionalization using differential shot noise and conductance in nonequilibrium states controlled by tunneling phases, *Phys. Rev. B* **105**, 205430 (2022).
- [31] L. Gruñeiro, M. Alvarado, A. L. Yeyati, and L. Arachéa, Transport features of a topological superconducting nanowire with a quantum dot: Conductance and noise, *Phys. Rev. B* **108**, 045418 (2023).
- [32] M. Trif and Y. Tserkovnyak, Resonantly tunable Majorana polariton in a microwave cavity, *Phys. Rev. Lett.* **109**, 257002 (2012).
- [33] M. C. Dartiailh, T. Kontos, B. Douçot, and A. Cottet, Direct cavity detection of Majorana pairs, *Phys. Rev. Lett.* **118**, 126803 (2017).
- [34] A. Cottet, T. Kontos, and B. Douçot, Squeezing light with Majorana fermions, *Phys. Rev. B* **88**, 195415 (2013).
- [35] M. Trif, O. Dmytruk, H. Bouchiat, R. Aguado, and P. Simon, Dynamic current susceptibility as a probe of Majorana bound states in nanowire-based Josephson junctions, *Phys. Rev. B* **97**, 041415(R) (2018).
- [36] L. Ricco, V. Kozin, A. Seridonio, and I. Shelykh, Accessing the degree of Majorana nonlocality in a quantum dot-optical microcavity system, *Sci. Rep.* **12**, 2045 (2022).
- [37] O. Dmytruk and M. Trif, Microwave detection of gliding Majorana zero modes in nanowires, *Phys. Rev. B* **107**, 115418 (2023).
- [38] D. Bathellier, L. Raymond, T. Jonckheere, J. Rech, A. Zazunov, and T. Martin, Finite frequency noise in a normal metal-topological superconductor junction, *Phys. Rev. B* **99**, 104502 (2019).
- [39] S. Smirnov, Majorana finite-frequency nonequilibrium quantum noise, *Phys. Rev. B* **99**, 165427 (2019).
- [40] R. M. Lutchyn, E. P. A. M. Bakkers, L. P. Kouwenhoven, P. Krogstrup, C. M. Marcus, and Y. Oreg, Majorana zero modes in superconductor-semiconductor heterostructures, *Nat. Rev. Mater.* **3**, 52 (2018).
- [41] E. Prada, P. San-Jose, M. W. A. de Moor, A. Geresdi, E. J. H. Lee, J. Klinovaja, D. Loss, J. Nygård, R. Aguado, and L. P. Kouwenhoven, From Andreev to Majorana bound states in hybrid superconductor-semiconductor nanowires, *Nat. Rev. Phys.* **2**, 575 (2020).
- [42] K. Flensberg, F. von Oppen, and A. Stern, Engineered platforms for topological superconductivity and Majorana zero modes, *Nat. Rev. Mater.* **6**, 944 (2021).
- [43] J. Barański, M. Barańska, T. Zienkiewicz, R. Taranko, and T. Domański, Dynamical leakage of Majorana mode into side-attached quantum dot, *Phys. Rev. B* **103**, 235416 (2021).
- [44] K. Wrześniewski and I. Weymann, Magnetization dynamics in a Majorana-wire-quantum-dot setup, *Phys. Rev. B* **103**, 125413 (2021).
- [45] K. Wrześniewski, B. Baran, R. Taranko, T. Domański, and I. Weymann, Quench dynamics of a correlated quantum dot sandwiched between normal-metal and superconducting leads, *Phys. Rev. B* **103**, 155420 (2021).
- [46] E. Vernek, P. H. Penteado, A. C. Seridonio, and J. C. Egues, Subtle leakage of a Majorana mode into a quantum dot, *Phys. Rev. B* **89**, 165314 (2014).
- [47] M. Cheng, M. Becker, B. Bauer, and R. M. Lutchyn, Interplay between Kondo and Majorana Interactions in Quantum Dots, *Phys. Rev. X* **4**, 031051 (2014).

- [48] J. F. Silva, L. G. G. V. D. da Silva, and E. Vernek, Robustness of the Kondo effect in a quantum dot coupled to Majorana zero modes, *Phys. Rev. B* **101**, 075428 (2020).
- [49] P. Majek, K. P. Wójcik, and I. Weymann, Spin-resolved thermal signatures of Majorana-Kondo interplay in double quantum dots, *Phys. Rev. B* **105**, 075418 (2022).
- [50] M. Lee, J. S. Lim, and R. López, Kondo effect in a quantum dot side-coupled to a topological superconductor, *Phys. Rev. B* **87**, 241402(R) (2013).
- [51] K. P. Wójcik and P. Majek, Majorana Coupling and Kondo Screening of Localized Spins, *Acta Phys. Pol. A* **143**, 207 (2023).
- [52] A. Ptok, A. Kobińska, and T. Domański, Controlling the bound states in a quantum-dot hybrid nanowire, *Phys. Rev. B* **96**, 195430 (2017).
- [53] N. Leumer, M. Marganska, B. Muralidharan, and M. Grifoni, Exact eigenvectors and eigenvalues of the finite Kitaev chain and its topological properties, *J. Phys.: Condens. Matter* **32**, 445502 (2020).
- [54] P. Majek, G. Górski, T. Domański, and I. Weymann, Hallmarks of Majorana mode leaking into a hybrid double quantum dot, *Phys. Rev. B* **106**, 155123 (2022).
- [55] G. S. Diniz and E. Vernek, Majorana correlations in quantum impurities coupled to a topological wire, *Phys. Rev. B* **107**, 045121 (2023).
- [56] K. G. Wilson, The renormalization group: Critical phenomena and the Kondo problem, *Rev. Mod. Phys.* **47**, 773 (1975).
- [57] R. Kubo, The fluctuation-dissipation theorem, *Rep. Prog. Phys.* **29**, 255 (1966).
- [58] M. Leijnse and K. Flensberg, Scheme to measure Majorana fermion lifetimes using a quantum dot, *Phys. Rev. B* **84**, 140501(R) (2011).
- [59] D. E. Liu and H. U. Baranger, Detecting a Majorana-fermion zero mode using a quantum dot, *Phys. Rev. B* **84**, 201308(R) (2011).
- [60] A. I. Tóth, L. Borda, J. von Delft, and G. Zaránd, Dynamical conductance in the two-channel Kondo regime of a double dot system, *Phys. Rev. B* **76**, 155318 (2007).
- [61] A. Płomińska, M. Misiorny, and I. Weymann, Spin-resolved dynamical conductance of a correlated large-spin magnetic molecule, *Phys. Rev. B* **95**, 155446 (2017).
- [62] O. Legeza, C. P. Moca, A. I. Toth, I. Weymann, and G. Zarand, Manual for the Flexible DM-NRG code, [arXiv 0809.3143](https://arxiv.org/abs/0809.3143) (2008). The code is available at <http://www.phy.bme.hu/~dmnrg/>.
- [63] A. I. Tóth, C. P. Moca, Ö. Legeza, and G. Zaránd, Density matrix numerical renormalization group for non-Abelian symmetries, *Phys. Rev. B* **78**, 245109 (2008).
- [64] F. B. Anders and A. Schiller, Real-time dynamics in quantum-impurity systems: A time-dependent numerical renormalization-group approach, *Phys. Rev. Lett.* **95**, 196801 (2005).
- [65] A. Weichselbaum and J. von Delft, Sum-Rule Conserving Spectral Functions from the Numerical Renormalization Group, *Phys. Rev. Lett.* **99**, 076402 (2007).
- [66] W. C. Oliveira and L. N. Oliveira, Generalized numerical renormalization-group method to calculate the thermodynamical properties of impurities in metals, *Phys. Rev. B* **49**, 11986 (1994).
- [67] F. D. M. Haldane, Scaling theory of the asymmetric Anderson model, *Phys. Rev. Lett.* **40**, 416 (1978).
- [68] D. A. Ruiz-Tijerina, E. Vernek, L. G. G. V. Dias da Silva, and J. C. Egues, Interaction effects on a Majorana zero mode leaking into a quantum dot, *Phys. Rev. B* **91**, 115435 (2015).
- [69] I. Weymann and K. P. Wójcik, Transport properties of a hybrid Majorana wire-quantum dot system with ferromagnetic contacts, *Phys. Rev. B* **95**, 155427 (2017).
- [70] J. Barański, M. Barańska, T. Zienkiewicz, J. Tomaszewska, and K. J. Kapcia, Continuous unitary transformation approach to the Kondo-Majorana interplay, *J. Magn. Magn. Mat.* **588**, 171464 (2023).
- [71] I. Weymann, K. P. Wójcik, and P. Majek, Majorana-Kondo interplay in T-shaped double quantum dots, *Phys. Rev. B* **101**, 235404 (2020).
- [72] K. T. Law, P. A. Lee, and T. K. Ng, Majorana Fermion Induced Resonant Andreev Reflection, *Phys. Rev. Lett.* **103**, 237001 (2009).
- [73] K. Flensberg, Tunneling characteristics of a chain of Majorana bound states, *Phys. Rev. B* **82**, 180516(R) (2010).
- [74] J. R. Schrieffer and P. A. Wolff, Relation between the Anderson and Kondo Hamiltonians, *Phys. Rev.* **149**, 491 (1966).
- [75] T. Domański, I. Weymann, M. Barańska, and G. Górski, Constructive influence of the induced electron pairing on the Kondo state, *Sci. Rep.* **6**, 23336 (2016).
- [76] M. Eckstein and P. Werner, Two-channel Kondo physics in a periodically driven single-impurity Anderson model (2017), [arXiv:1704.02300](https://arxiv.org/abs/1704.02300) [cond-mat.str-el].
- [77] V. Bruch, M. Pletyukhov, H. Schoeller, and D. M. Kennes, Floquet renormalization group approach to the periodically driven Kondo model, *Phys. Rev. B* **106**, 115440 (2022).
- [78] V. L. Quito and R. Flint, Floquet engineering multichannel Kondo physics, *Phys. Rev. B* **108**, 155120 (2023).
- [79] N. Dasari and M. Eckstein, Transient Floquet engineering of superconductivity, *Phys. Rev. B* **98**, 235149 (2018).
- [80] M. M. Maška, A. Gorczyca-Goraj, J. Tworzydło, and T. Domański, Majorana quasiparticles of an inhomogeneous Rashba chain, *Phys. Rev. B* **95**, 045429 (2017).
- [81] M. T. Deng, S. Vaitiekėnas, E. B. Hansen, J. Danon, M. Leijnse, K. Flensberg, J. Nygård, P. Krogstrup, and C. M. Marcus, Majorana bound state in a coupled quantum-dot hybrid-nanowire system, *Science* **354**, 1557 (2016).
- [82] L. Schneider, K. T. Ton, I. Ioannidis, J. Neuhaus-Steinmetz, T. Posske, R. Wiesendanger, and J. Wiebe, Proximity superconductivity in atom-by-atom crafted quantum dots, *Nature* **621**, 60 (2023).
- [83] P. Zellekens, R. S. Deacon, P. Perla, D. Grützmacher, M. I. Lepsa, T. Schäpers, and K. Ishibashi, Microwave spectroscopy of Andreev states in InAs nanowire-based hybrid junctions using a flip-chip layout, *Communications Physics* **5**, 267 (2022).